Environmental Fluid Mechanics (2020) 20:1053–1073
https://doi.org/10.1007/s10652-020-09740-y

ORIGINAL ARTICLE

Transient secondary currents behind a compression wave in an irregular channel

Urvisha Kiri[1] · Xinqian Leng[1,2] · Hubert Chanson[1]

Received: 18 March 2018 / Accepted: 20 March 2020 / Published online: 10 April 2020

Abstract
A compression wave is an unsteady rapidly-varied open channel flow motion, characterised by an increase in water depth. A detailed investigation was conducted in a prismatic asymmetrical channel, to better understand the physical processes observed in tidal/tsunami-bore affected estuaries with irregular topography. The prismatic channel was equipped with a 1 V:5H transverse slope across the full channel width. The free-surface data presented three-dimensional unsteady flow features, and the velocity measurements showed a drastic impact of the surge on the flow field, with strong three-dimensional features. With the arrival of the surge front, the transverse velocity component became large in the shallow-water section, indicating some unsteady secondary motion and recirculation during and shortly after the passage of the surge. The Reynolds shear stress data were associated with large turbulent stresses and shear stress fluctuations. For $d_1/D < 1$, both velocity and shear stress data showed a transient longitudinal x–z shear plane, about y/W 0.5–0.6, with conjugate transverse flow reversal for $0.5–0.6 < y/W < 1$. In the transient shear plane, high Reynolds stress magnitudes and shear stress fluctuations were observed behind the surge front, up to one to two orders of magnitude larger than boundary shear stress levels observed in steady flows in compound channels.

Keywords Transient secondary currents · Compression waves · Turbulent Reynolds stresses · Transient shear plane · Physical modelling

1 Introduction

A compression wave, also called positive surge or hydraulic jump in translation, is an unsteady rapidly-varied open channel flow motion, characterised by an increase in water depth [17]. Positive surges constitute hydrodynamic shocks, linked to a discontinuity in terms of the

Electronic supplementary material The online version of this article (https://doi.org/10.1007/s10652-020-09740-y) contains supplementary material, which is available to authorized users.

✉ Hubert Chanson
h.chanson@uq.edu.au

1 School of Civil Engineering, The University of Queensland, Brisbane, QLD 4072, Australia

2 Present Address: I2M, Laboratory TREFLE, Université de Bordeaux, Pessac, France

pressure and velocity fields [29, 41], as illustrated in Figs. 1 and 3a. The shock propagation is associated with intense unsteady turbulence [18, 25]. Environmental applications of positive surges include tidal bores in estuaries and in-river tsunami bores [6, 43, 45]. The surge propagation is associated with intense mixing, and sediment upwelling and suspension, as observed in tidal bore affected estuaries [11, 16, 20]. The development of a compression wave, its inception and its propagation may be predicted analytically and numerically [1, 2, 17, 19]. After formation, the flow properties upstream and downstream of the surge front must fulfil the equations of conservation of mass and momentum in their respective integral form [7, 14, 29]:

Past investigations of positive surges were mostly conducted in rectangular channels (e.g. [15, 18, 24], except for a few free-surface measurements in symmetrical trapezoidal channels [4, 37]. Herein both free-surface and velocity measurement experiments were performed in a large-size flume with a non-rectangular asymmetrical cross-section. The present investigation focused on the unsteady turbulent properties of the three-dimensional flow and the transverse mixing induced by unsteady secondary motion.

2 Theoretical considerations

2.1 Presentation

When a compression wave propagates upstream, the response of the flow to the passage of the wave leading edge may be analysed as an impulse problem [29]. The forcing is the longitudinal pressure gradient across the surge front, as illustrated in Fig. 1. Let us consider the forced solution for a quasi-steady compression wave (Fig. 1, bottom) [17, 19]. Focusing on the initial impulse, the surge suddenly arrives at t = 0. In a system of reference in translation with the compression wave front, the depth-integrated equations of conservation of mass and momentum are, with the hydrostatic assumption:

$$\frac{\partial q_x}{\partial x} + \frac{\partial q_y}{\partial y} = -\frac{\partial d}{\partial t} \tag{1}$$

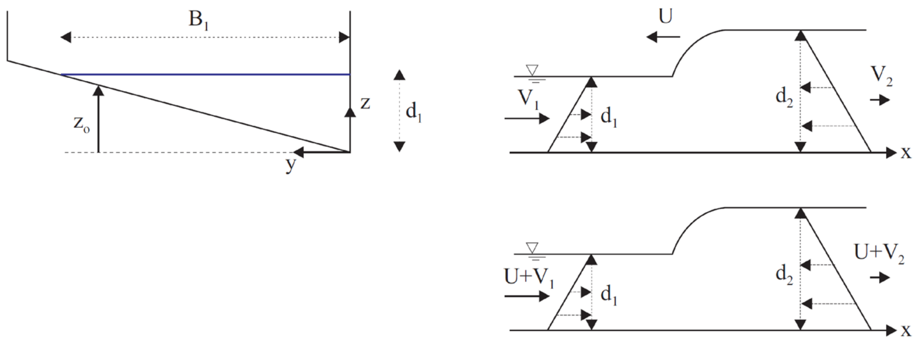

Fig. 1 Definition sketch of a compression wave propagating upstream and the associated longitudinal pressure gradient induced forcing

$$\frac{\partial q_x}{\partial t} = -g \times d \times \frac{\partial d}{\partial x} + \frac{F_x}{\rho} \tag{2A}$$

$$\frac{\partial q_y}{\partial t} = -g \times d \times \frac{\partial d}{\partial y} \tag{2B}$$

where q_x and q_y are the depth-integrated unit discharges in the longitudinal and transverse directions, i.e. $q_x=(V_x+U)d$ and $q_y=V_yd$, d is the water depth, g is the gravity acceleration, ρ is the water density, and the longitudinal forcing F_x is the net pressure force. Assuming hydrostatic pressure distributions in front of and behind the compression wave, the net pressure force resultant consists of the increase of pressure $\rho \times g \times (d_2 - d_1)$ applied to the initial flow cross-section area A_1 plus the pressure force on the cross-section area $(A_2–A_1)$:

$$\begin{aligned} F_x &= \iint_{A_1} P \times dA - \iint_{A_2} P \times dA \\ &= \int_{y=0}^{B} \rho \times g \times (d_1 - d_2) \times (d_1 - z_o) \times dy - \int_{y=0}^{B} \frac{1}{2} \times \rho \times g \times (d_2 - d_1)^2 \times dy \end{aligned} \tag{3}$$

with F_x positive downstream, B the free-surface width, and the subscripts 1 and 2 referring to the initial and conjugate flow conditions (Fig. 1).

A solution to an impulse forcing may be developed, following CSANADY [13], assuming that q_x is a linear function of time:

$$q_x = \alpha \times t + (U + V_1) \times d \text{ for t } > 0 \tag{4}$$

and q_y is zero. In a prismatic channel, the velocity may be assumed to be longitudinal and the transverse transport is small. At any instant and longitudinal position, the application of the equation of conservation of mass in an integral form imposes:

$$\int_{y=0}^{B} q_x \times dy = (V_1 + U) \times A_1 = (V_2 + U) \times A_2 = \text{constant} \tag{5}$$

Using Eq. (4), it gives

$$\int_{y=0}^{B} \alpha \times dy = 0 \tag{6}$$

A complete expression of the longitudinal unit discharge is then:

$$q_x = (U + V_x) \times d = F_x \times t \times \left(1 - \frac{d \times B_1}{A_1}\right) + (U + V_1) \times d \quad \text{for} \quad \text{t} > 0 \tag{7}$$

where the water depth d is a function of the transverse coordinate, B_1 is the initial free-surface width and A_1 is the initial flow area (Fig. 1). Equation (7) provides a simple expression of the relative longitudinal velocity focusing on the initial instants of the arrival of the compression wave, in a prismatic channel. It may be rewritten in terms of depth-averaged velocity q_x/d at a transverse location:

$$\frac{q_x}{d} = \frac{F_x \times t}{d} \times \left(1 - \frac{d \times B_1}{A_1}\right) + V_1 \text{ for t } > 0 \tag{8}$$

Equations (1)–(8) were developed for an irregular channel, irrespective of the shape. They are general enough to be applicable to wide range of channel cross-sections, subjected to an impulse forcing caused by a longitudinal pressure force, e.g. linked to very-rapid increase in water level during the passage of the compression wave.

2.2 Application

The simple relationship in Eqs. (8) is illustrated in Fig. 2, using the depth distribution of a 1 V:5H channel. The transverse distribution of the depth-averaged longitudinal velocity is clearly a related to the depth distribution. The longitudinal velocity q_x/d is equal to the initial cross-sectional-averaged velocity V_1 when $d = A_1/B_1$, which is the average depth of the section [7, 17].

The transverse distribution of longitudinal velocity in the channel subjected to a compression wave may now be elucidated qualitatively. Recalling Eq. (8), the solution yields a positive longitudinal flow in the deep water section of the channel, during the impulse forcing corresponding to the passage of the compression wave. In the shallow water region, the longitudinal velocity becomes negative. The details depend on the flow conditions, but the appearance of a "gyre" pattern follows, as illustrated in Fig. 2. Figure 2 shows the calculated pattern for sudden longitudinal pressure forcing applies from $t > 0$. The transverse profile is asymmetrical, and agrees with the qualitative inference from dye injection experiments (Appendix I). The gyre is indeed related to the transverse bed profile. Near the outer edge of the shallow water section, a singularity occurs on account of the depth d reducing to zero. In very shallow water, it is not realistic to neglect friction even for a short initial period. The velocity distribution is noteworthy in that it shows the development of transverse velocity profile with time, albeit the present development is only valid over a very short time frame.

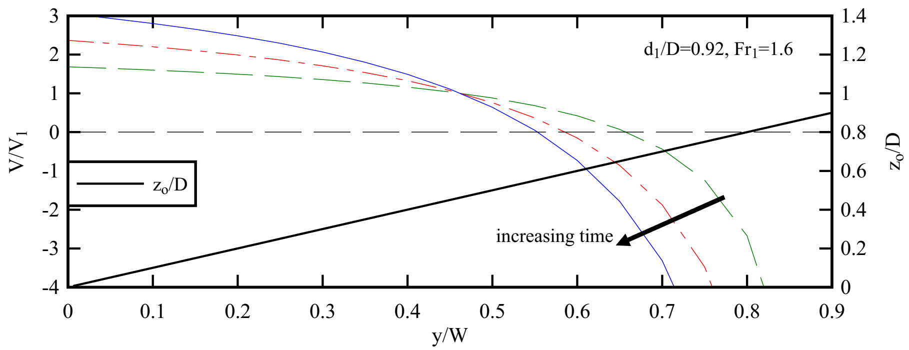

Fig. 2 Transverse distribution of dimensionless longitudinal velocity $q_x/(V_1 d)$ for an impulse forcing imposed by a longitudinal pressure gradient during the passage of a compression wave in a channel with a 1 V:5H transverse slope

3 Physical modelling

3.1 Presentation

Although physical models are geometrically-scaled based upon prototypes, geometric similarity is not sufficient and any investigation requires some similarity in flow patterns [17]. Considering a compression wave propagation in an asymmetrical channel (Fig. 3c), the most relevant parameters are the fluid properties, channel geometry, physical constants and inflow conditions [17, 28]. A simplified dimensional analysis yields a series of dimensionless relationships between the instantaneous turbulent flow properties, at a position (x,y,z) and time t, and key relevant parameters:

$$\frac{d}{\frac{A_1}{B_1}}, \frac{V_x}{V_1}, \frac{V_y}{V_1}, \frac{V_z}{V_1}, \frac{P}{\rho \times g \times \frac{A_1}{B_1}}, \frac{\tau_{ij}}{\rho \times V_1^2}, \ldots = F\left(\frac{x}{\frac{A_1}{B_1}}, \frac{y}{\frac{A_1}{B_1}}, \frac{z}{\frac{A_1}{B_1}}, t \times \sqrt{\frac{g}{\frac{x}{\frac{A_1}{B_1}}}}, \frac{d_1}{D}, \frac{W}{D}, \frac{k_s}{\frac{A_1}{B_1}}, \theta, \frac{U + V_1}{\sqrt{g \times \frac{A_1}{B_1}}}, \rho \times \frac{(U + V_1) \times \frac{A_1}{B_1}}{\mu}, \frac{g \times \mu^4}{\rho \times \sigma^3}, \ldots \right) \tag{9}$$

where V_x, V_y and V_z are the instantaneous longitudinal, transverse and vertical velocity components respectively, P is the instantaneous pressure, τ_{ij} is the instantaneous Reynolds stress component with i,j = x, y, or z, x is the longitudinal coordinate positive downstream, y is the transverse coordinate measured from the right sidewall, z is the vertical coordinate with z = 0 at the lowest bed elevation, t is the time, D is the transverse bed elevation difference between left and right sidewalls, W is the full width of the flume, k_s is the equivalent sand roughness height of the bed, θ is the angle of the longitudinal channel bed and the horizontal, U is the bore celerity positive upstream, ρ is the fluid density, μ is the dynamic viscosity of the fluid, and σ is the surface tension. In Eq. (9), the relevant characteristic length and velocity scales are the initial equivalent flow depth A_1/B_1 and velocity V_1, based upon momentum considerations. It should be noted that the compression wave is assumed to be a monophase flow, and the biochemical properties of the fluid and sediment characteristics in natural systems are not considered in Eq. (9).

In the right hand side of Eq. (9), the 9th term is the surge Froude number Fr_1, the 10^{th} term is the surge Reynolds number Re_1 and 11 th term is the Morton number Mo which is a function of the fluid properties and gravity constant only. In the physical modelling of hydraulic jumps and compression waves, a Froude similitude is derived theoretically from momentum considerations [7, 17]. The Morton number is equal in laboratory and prototype when the same fluids are used during the physical study and at full scale. In turn, viscous effects might take place in small laboratory channels, because the Reynolds similitude cannot be achieved. Herein, the experimental study was conducted based upon Froude and Morton similitudes, using relatively large Reynolds numbers ranging from 7.510^4 to 310^5, since a large-size facility was used.

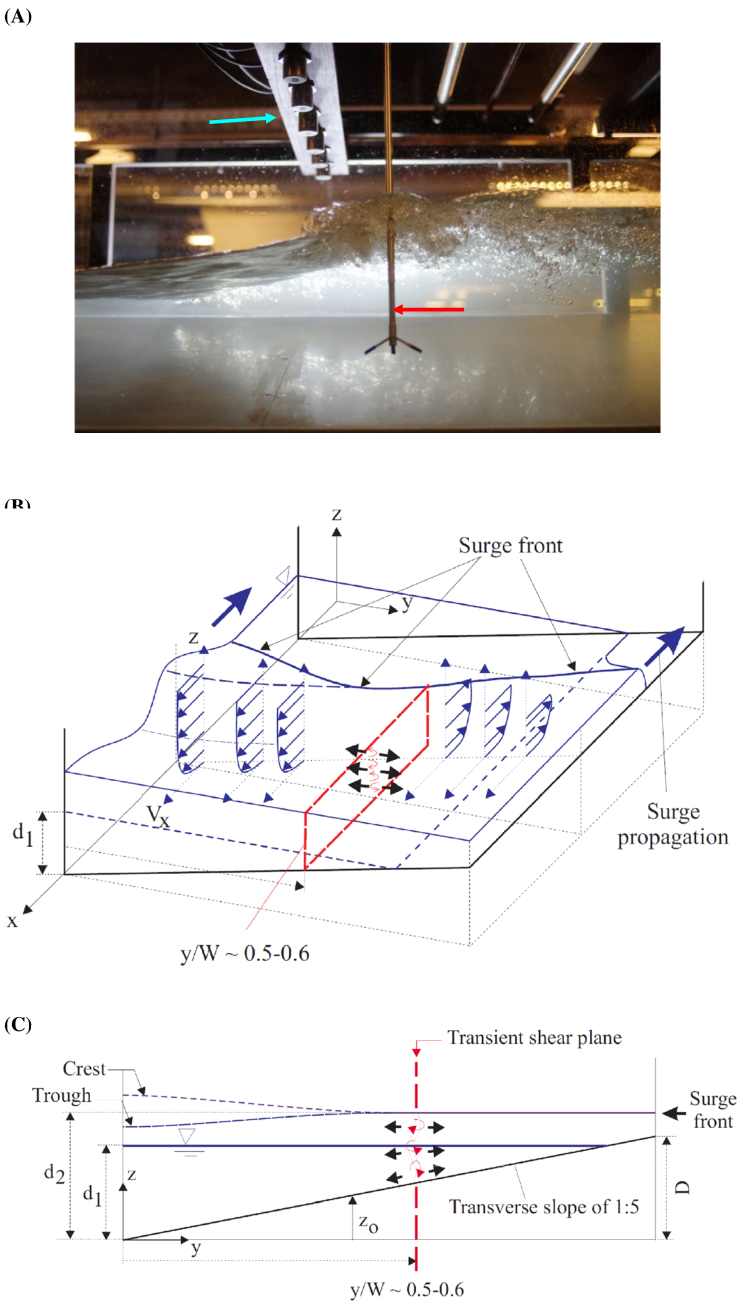

Fig. 3 Compression wave propagation in a non-rectangular asymmetrical channel. **a** Surge propagation from right to left—view through the right sidewall, with an series acoustic displacement meter (ADM) units (light blue arrow) mounted above the free-surface across the channel width and an acoustic Doppler velocimeter (ADV) Vectrino II Profiler (red arrow) sampling beneath the surge front. **b** Three-dimensional sketch of compression wave and conjugate flow motion behind the surge front. **c** Cross-sectional view looking upstream

3.2 Experimental facility and instrumentation

New experiments were conducted in a 19 m long and 0.7 m wide rectangular tilting flume equipped with 0.52 m high glass sidewalls, previously used by [25, 26]. The channel bed was modified by the installation of a 1 V:5H transverse slope, made out of PVC (Fig. 3). The 1 V:5H transverse slope extended for the full breadth of the channel as sketched in Figs. 1b and 3b, with the deep section along the right sidewall. The transverse slope invert was installed between x = 2 m and 17 m. Smooth transitions from rectangular to trapezoidal cross-sections, and from trapezoidal to rectangular cross-sections, were installed at x < 2 m and x > 17 m, where x is the longitudinal distance from the start of the flume, positive downstream. Water flow was supplied at a steady rate by an upstream water tank, followed by a series of flow straighteners and smooth convergent. A fast-closing Tainter gate was located at the channel's downstream end (x = 18.1 m). A movie of the surge propagation is presented in Appendix I (Movie CIMG3470.mov). The channel slope was constant for all experiments ($S_o = 0.002216$).

The water discharge was measured using a magneto-flow meter. In steady flows, the free-surface elevations were measured using rail mounted pointer gauges. The velocity measurements were conducted with a Dwyer® 166 Series Prandtl-Pitot tube (= 3.18 mm) and a Nortek™ acoustic Doppler velocimeter (ADV) Vectrino II Profiler (Serial number P27338, Hardware ID VNO 1366).

The unsteady free-surface water elevations were recorded using non-intrusive acoustic displacement meters (ADMs) Microsonic™ Mic + 25/IU/TC and Microsonic™ Mic + 35/IU/TC, as shown in Fig. 3a. The three-dimensional surge flow pattern was recorded using ten ADMs, with two ADMs along the centreline at x = 6.96 m and x = 9.96 m, and six ADMs at x = 8.5 m, spaced evenly in the transverse direction, and two ADMs placed immediately upstream and downstream of the Tainter gate to record the gate closure time. All ADM sensors were calibrated against rail mounted pointer gauge water depth data. For each unsteady experiment, the free-surface elevation measurements were sampled at 100 Hz.

Unsteady velocity measurements were conducted using the Nortek™ acoustic Doppler velocimeter Vectrino II Profiler (Serial number P27338, Hardware ID VNO 1366) in the deep-water sections of the channel and a Nortek™ acoustic Doppler velocimeter Vectrino + (Serial No. VNO 0436) in the shallow-water sections. The ADV Profiler was equipped with a three-dimensional down-looking head, capable of taking simultaneous velocity measurements in a 30 mm profiling range at 1 mm increments. (The physical experiments were conducted in 2017, after a manufacturer's re-calibration in January 2017.) The velocity range was set at 1.0 m/s for the lowest flow rates and 1.2 m/s for the higher flow rates. The ADV Vectrino + was equipped with a side-looking head and recorded velocity measurements at a single point. The velocity range was set at 1.0 m/s. The ADV mount was installed at x = 8.6 m. For each experiment, the velocity measurements were sampled at 100 Hz for the ADV Profiler and at 200 Hz for the ADV Vectrino +.

The ADV signals were post-processed in steady flows [21]. The unsteady velocity measurements were not post-processed, behind a careful synchronisation for ensemble-averaging.

3.3 Experimental flow conditions

The steady flow conditions were characterised through a series of experiments for three discharges: Q = 0.015 m^3/s, 0.050 m^3/s and 0.1017 m^3/s. Detailed measurements included free-surface elevations, velocity distributions, and Reynolds shear stress distributions at x = 8.6 m for several transverse locations y.

Unsteady flow experiments were conducted to characterise the changes in velocity and free-surface profile during the passage of the bore at x = 8.6 m. This included experiments at various vertical and transverse locations along the channel cross section for a range of flow conditions (Table 1). In Table 1, Q is the initially steady flow rate, Re_1 is the surge Reynolds number, h is the gate opening after closure, d_1 is the initial steady flow water depth measured along the right sidewall, y is the transverse location, $(z-z_o)$ is the local elevation above the bed and z_o is the bed elevation at a transverse location y. All present

Table 1 Summary of positive surge experiments in a non-rectangular asymmetrical channel

Q m^3/s	Re_1	h m	d_1 m	Fr_1	y m	$z-z_o$ m	Instrumentation
0.030	$7.5\,10^{4}$	0	0.13	1.59–1.63	0.050	0.006–0.035	ADV Profiler
					0.100		
					0.200		
					0.050	0.031–0.060	
					0.350	0.006 0.021 0.041	ADV Vectrino +
					0.400	0.006	
					0.450	0.006 0.024	
					0.500	0.006	
					0.550	0.006	
	$6.6\,10^{4}$	0.016		1.36	N/A	N/A	ADM only
0.050	$1.3\,10^{5}$	0	0.156	1.63	N/A	N/A	ADM only
0.055	$1.4\,10^{5}$	0	0.164	1.53–1.64	0.050	0.006–0.035 0.051–0.080	ADV Profiler
					0.100	0.006–0.035 0.051–0.080	
					0.200	0.006–0.035	
					0.300	0.006–0.035	
	$1.2\,10^{5}$	0.032	0.164	1.30–1.34	0.050	0.006–0.035 0.051–0.080	ADV Profiler
					0.100	0.006–0.035 0.051–0.080	
					0.200	0.006–0.035	
					0.300	0.006–0.035	
0.100	$3\,10^{5}$	0	0.209	1.60–1.80	0.100	0.006–0.035 0.76–0.105	ADV Profiler
					0.350	0.006–0.035	
					0.450	0.006–0.035	
	$1.7\,10^{5}$	0.055	0.209	1.30	N/A	N/A	ADM Only

d_1: water depth measured next to right sidewall; Fr_1: surge Froude number: $Fr_1 = (V_1 + U)/(gA_1/B_1)^{1/2}$; Re_1: surge Reynolds number: $Re_1 = \rho(V_1 + U)A_1/B_1/\mu$; S_o: bed slope ($S_o = 0.002216$); z_o: local bed elevation; Unless stated, all experiments included ADM measurements experiments were conducted with relatively large Reynolds numbers, ranging from 7.510^4 to 310^5, to minimise potential scale effects.

The positive surge was generated by closing rapidly the Tainter gate, and the surge propagated upstream until it reached the intake structure. Sampling was stopped once the surge reached x = 0 m. The Tainter gate closure time was less than 0.15–0.2 s [25] and had a negligible effect on the propagation of the surge. For each flow condition, the unsteady flow experiments were repeated 25 times, the ADM and ADV data were synchronised within 1 ms, and the results were ensemble-averaged following CHANSON and DOCHERTY [10] and [25, 26]. Based upon the data ensembles, the instantenous median and fluctuations were obtained. The latter was calculated as the interquartile range, or difference between third and first quartiles.

Herein, a number of experimental cases were selected to cover a wider range of conditions, including to compare differences depending upon the initial flow cross-sectional shape (triangular or trapezoidal). The results showed a drastic impact of the cross-sectional shape, i.e. triangular for $d_1/D < 1$ or trapezoidal for $d_1/D > 1$ (Sect. 4). For a limited number of cases, the experiments were repeated 25 times in the current study and an ensemble statistical analysis was conducted to extract mean and fluctuating quantities. Such a rigorous methodology is difficult to achieve high quality data sets [9]. In turn, the approach restricted the spatial coverage of the data, and the secondary flow maps could not be generated with the current metrology.

4 Steady open channel flow properties

Steady flow measurements were conducted at various longitudinal and transverse locations. The free-surface was horizontal in the transverse direction for all flow conditions. The free-surface was basically parallel to the longitudinal bed, i.e. d/x = 0, indicating uniform-equilibrium flow conditions. For the smallest flow rate ($Q = 0.015$ m^3/s), the channel cross-section was triangular with $d < D$, where d is the steady flow depth measured at x = 8.6 m. For the larger flow rates, the channel cross-section was trapezoidal. The application of the momentum equation for uniform-equilibrium flows provided a quantitative estimate of the cross-sectional average boundary shear stress. The results yielded a dimensionless shear stress The Darcy-Weisbach friction factor is related to the boundary shear stress as: $f = 8\tau_o/(\rho V_{mean}^2)$ between 0.016 and 0.018 depending upon the discharge, where V_{mean} is the cross-sectional average velocity.

At the sampling cross-section (x = 8.6 m), the velocity data showed that the flow was three-dimensional, owing to the asymmetrical shape of the channel cross-section. Figure 4 presents typical velocity profiles measured using a Prandtl-Pitot tube and ADV unit for one discharge at two transverse locations. The experimental data are compared to the theoretical log-wake law velocity profile [8, 32, 38]. In Fig. 4, the local bed elevation z_o is shown with a black dashed line and the free-surface elevation is the thick blue horizontal line. Overall, there was a close agreement between Pitot tube and ADV data, as well as between physical data and theory. The velocity data fulfilled the no-slip boundary condition: that is, the longitudinal velocity was zero at the bed: $V_x(z = z_o) = 0$. The steady flow was fully developed and three-dimensional at the sampling location. Within the lower flow region, the vertical distributions of longitudinal velocity component followed a power law profile (Fig. 4). Next to the free-surface in the deep-water parts of the cross-section, a velocity dip was observed, with the maximum velocity recorded below the free-surface: e.g., at z/d 0.74 in Fig. 4 (Left). This phenomenon is believed

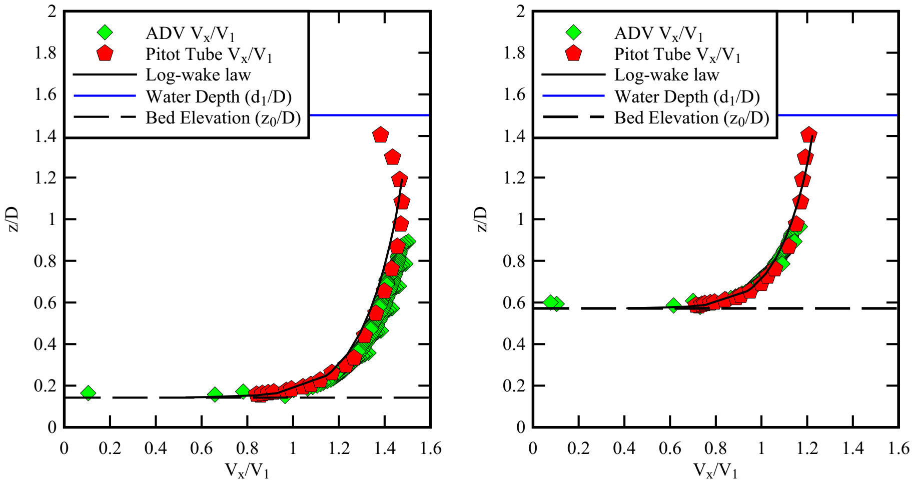

Fig. 4 Vertical profiles of time-averaged longitudinal velocity—Flow conditions: Q = 0.1017 m^3/s, d = 0.209 m, x = 8.6 m, y = 0.100 m (Left) and y = 0.400 m (Right)—Comparison between Prandtl-Pitot tube, ADV Profiler data and theoretical log-wake law

to be linked to intense secondary motion and transverse momentum exchange [34]. Further the Prandtl-Pitot tube measurements showed hydrostatic pressure distributions.

Detailed contours plots of the time-averaged longitudinal velocity were derived. Figure 5 presents typical examples. The velocity contour plots were integrated to yield the cross sectional flow rate:

$$\iint_A V_x \times dy \times dz \tag{10}$$

The results (Eq. (10)) were in close agreement with the discharge measurements within 3.5% [21]. The velocity contour plots showed that the velocity was not uniformly distributed. For d/D < 1, the flow cross-section was triangular (Fig. 5a) and low velocity areas were observed along the wetted perimeter. The highest velocity region was towards the triangle's centre about y/W = 0.2, where W is the full channel width (W = 0.7 m), as previously reported for a triangular channel [12]. For d/D > 1, the flow cross-section was trapezoidal and the patterns were asymmetrical, with two distinct regions of high velocity regions observed at y/W 0.2 and y/W 0.6 respectively (Fig. 5b). This may be associated with the existence of streamwise vortices, as a result of momentum transfer from high velocity regions to low velocity regions, previously documented in laboratory and in the field [35, 42, 44].

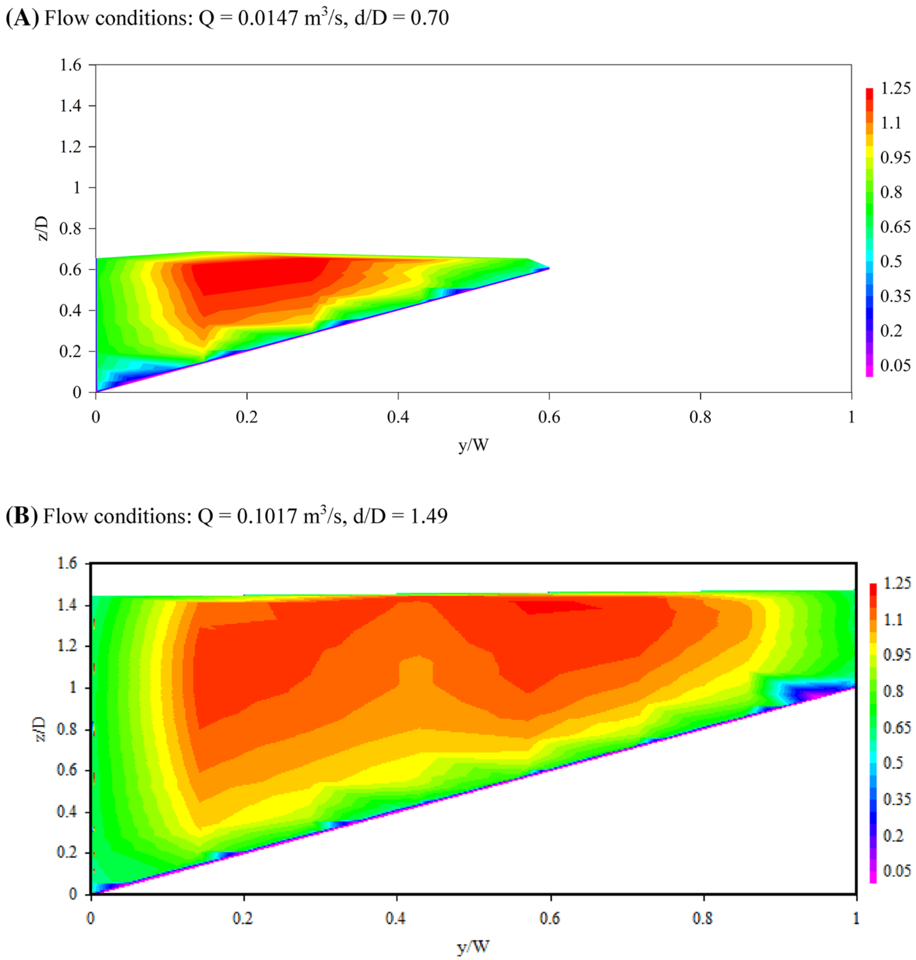

Fig. 5 Longitudinal velocity contour plots in steady flow at x = 8.6 m—Colour scale corresponds to V_x/V_1.. **a** Flow conditions: Q = 0.0147 m^3/s, d/D = 0.70. **b** Flow conditions: Q = 0.1017 m^3/s, d/D = 1.49

5 Unsteady flow properties: (1) Free-surface and velocity measurements

5.1 Free-surface flow patterns

The propagation of compression waves is a highly turbulent and unsteady process [18]. A series of ensemble-average measurements were conducted to study the free-surface and velocity characteristics during the passage of the positive surge. Typical outputs encompassed the median velocity V_{50}, median free-surface elevation d_{50}, and characteristic fluctuation in velocity V_{75-25} and free-surface elevation d_{75-25}, defined in terms of the interquartile range. For a Gaussian distribution of an ensemble around its mean, the interquartile range, e.g. $V_{75-25} = V_{75} - V_{25}$, would be equal to 1.3 times the standard deviation [40].

The water surface data showed that the passage of the compression wave was associated with a sudden rise of free-surface elevation, together with a marked increase in free-surface fluctuations. Figure 6 presents a typical data set, where t is the time since Tainter gate closure and y/W is the dimensionless transverse location. After the passage of the wave front, the free-surface fluctuations remained large, likely because of the complicated transverse motion and secondary currents observed on the asymmetrical bed configuration.

Visual observations showed different surge feature depending upon the surge Froude number and initial relative depth. For $Fr_1 > 1.5$ and $d_1/D > 1$, the positive surge was breaking and the roller region was quasi-two-dimensional. For all other flow conditions (Table 1), the surge was undular in the deeper side, albeit some breaking was observed towards the left side where the water was shallower. The surge leading edge arrived first in the shallow water side and trailed in the deep water. A complicated conjugate flow motion was observed behind the bore front, with transient secondary currents and surface scars in the wake of the shallow-water bore front (Digital Appendix I, movie CIMG3470.mov). For $d_1/D < 1$, visual observations highlighted strongly three-dimensional features, with transverse mixing illustrated by large-scale vortices and surface scars behind the surge front.

5.2 Velocity observations

The passage of the compression wave had a marked effect on the velocity field at all transverse and vertical positions for all flow conditions. This is illustrated in Fig. 7, showing typical dimensionless time variations of longitudinal and transverse velocity component during the passage of the surge at several transverse and vertical locations. In Fig. 7, Vx, $50/V_1$ is the dimensionless ensemble-median longitudinal velocity component, $V_{y,50}/V_1$ is the dimensionless ensemble-median transverse velocity component, d_{50}/d_1 is the dimensionless ensemble-median water elevation, $t(g/(A_1/B_1)^{0.5}$ is the dimensionless time.

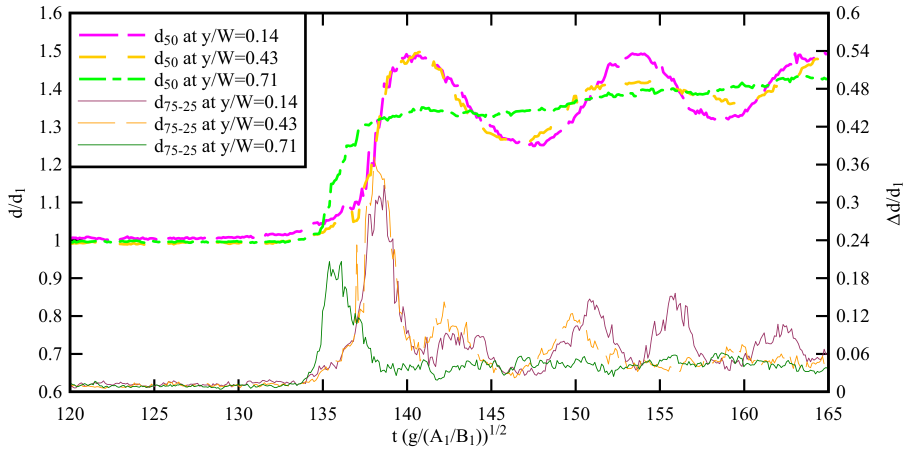

Fig. 6 Dimensionless time variation of median water elevation and water surface fluctuations at several transverse locations and at x = 8.6 m—Flow conditions: $Fr_1 = 1.57$, $Q = 0.0548$ m³/s, h = 0 m, $d_1 = 0.164$ m

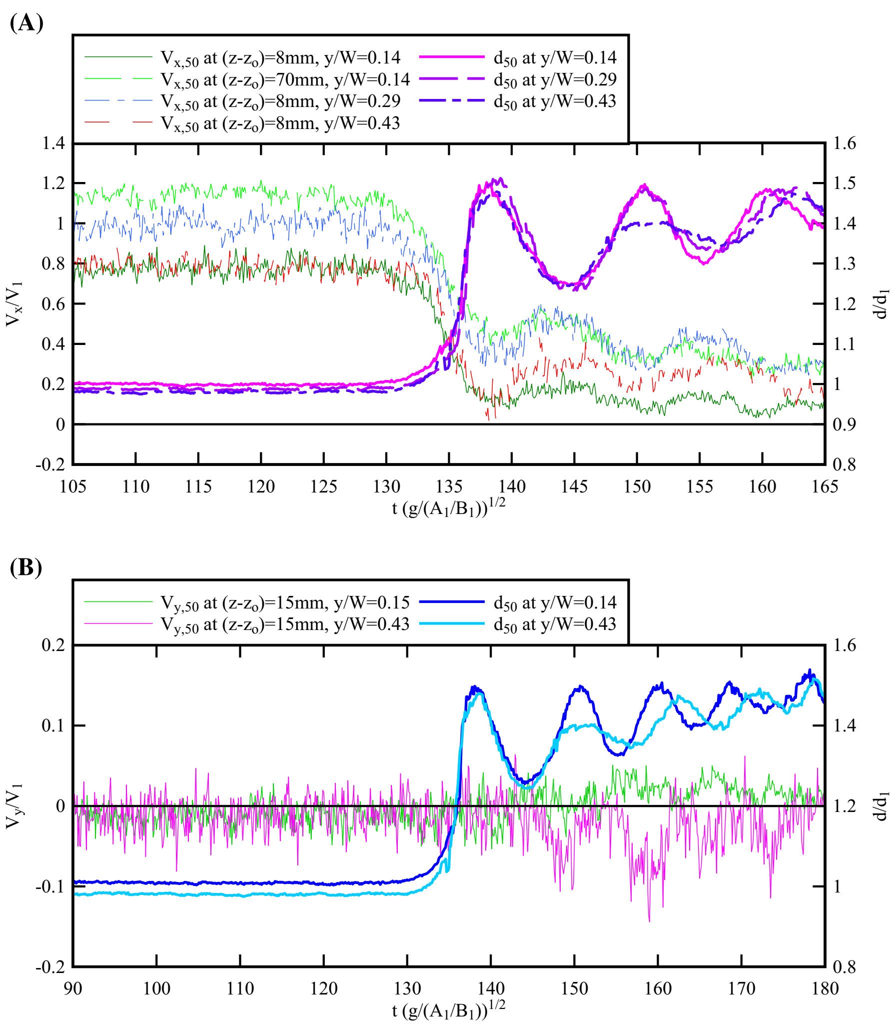

Fig. 7 Time variations of ensemble-median water elevation and velocity components at multiple transverse and vertical locations at x = 8.6 m during positive surge passage—Flow conditions: Q = 0.055 m^3/s, h = 0 m, Fr_1 = 1.53–1.57. **a** Longitudinal velocity component. **b** Transverse velocity component

The arrival of the positive surge was associated with a marked increase in water depth and decrease in the longitudinal velocity component. For all breaking bores, the longitudinal deceleration was abrupt and rapid, coinciding with the sharp increase in the water elevation at the roller toe. After the passage of the breaking surge, the longitudinal velocity was almost constant with large fluctuations, as the conjugate water depth steadied. For undular surges, the longitudinal velocity showed a more gradual deceleration at the arrival of the surge front, associated with the slower rate of rise in free-surface elevation. During the passage of the free-surface undulations, the longitudinal velocity oscillated about a mean value. Here, the longitudinal velocity measurements were maximum beneath the wave troughs and minimum at the wave crests, as seen in Fig. 7a.

The vertical velocity component followed a pattern similar to that observed for the free-surface elevation. Initially oscillating about zero, the vertical velocity V_z experienced a sharp increase at the arrival of a breaking surge, before returning to zero after the surge front. During the passage of the undular bore, the vertical velocity component increased at the arrival of the bore front and then the vertical velocity oscillated about zero in a quasi-periodic manner with the same period but out of phase with the free-surface elevation. A basic flow net theory in the frame of reference in translation with the surge front tends to validate the horizontal and vertical velocity component redistributions in the water column when the free-surface is a streamline [33, 36].

The time-variations of transverse velocity component differed across the channel width, as seen in Fig. 7b. For a given discharge, at $y/W=0.14$, the transverse velocity component showed small oscillations about $V_y/V_1=0$, while, at $y/W=0.43$ the transverse velocity was negative, and oscillated about $-0.05V_1$. The different behaviour might be induced by a combination of the transverse slope gravity effect and transverse and vertical momentum transfers across the channel.

A different flow motion was observed for the smallest discharge ($Q=0.030$ m^3/s) corresponding to $d_1/D<1$. This is illustrated in Fig. 8A, showing the longitudinal velocity component during the passage of the surge at several transverse locations. Following the arrival of the surge in the deep-water section, i.e. $y/W<0.64$, a gradual deceleration down to $V_x/V_1=0$ was observed, as previously reported for all larger discharges. For $y/W>0.64$, the rapid longitudinal deceleration was stronger, and the longitudinal velocity V_x became negative, with transient negative velocities downs to $-0.75V_1$ at $y/W=0.71$ and $-0.5V_1$ at $y/W=0.57$ (Fig. 8a). This pattern indicated a full flow reversal in the shallow section behind the positive surge, as well as a transient longitudinal shear zone about y/W 0.5–0.6. Such a location is marked with a blue dot in Fig. 8b. For $d_1/D<1$, the velocity measurements were complemented by visual observations including video movies. Visualisations using dye injection (Digital Appendix I, movie CIMG3470.mov) showed drastically different flow motions across the channel cross-section. In the deep-water section, the flow motion remained downstream whereas, in the shallower section, there was a reversal in flow direction with upstream dye advection behind the surge, as shown in Fig. 8b. Figure 8b presents three successive photographs taken immediately behind the surge front; on the right, the dye plume continued to flow downstream after the surge, whereas the dye flowed upstream in the shallow-water section on the left. The present results were consistent with theoretical considerations (Sect. 2, Fig. 2) and field observations. In many natural estuaries, the bore passage is associated with a strong flow reversal in the shallow sections [3, 22], The circulation patterns may indeed be related to the transverse bed profile (Eq. (8)).

5.3 Discussion

The instantaneous velocity fluctuation is a measure of turbulence and energy levels during the passage of the positive surge. In the present study, the arrival of the compression wave was associated with a marked increase in fluctuations of all velocity components. Close to the bed, a marked peak in longitudinal velocity fluctuation was recorded. This peak generally occurred at the time for which the greatest rate of change in velocity was observed. Next to the free-surface, the velocity fluctuations showed a gradual increase following the

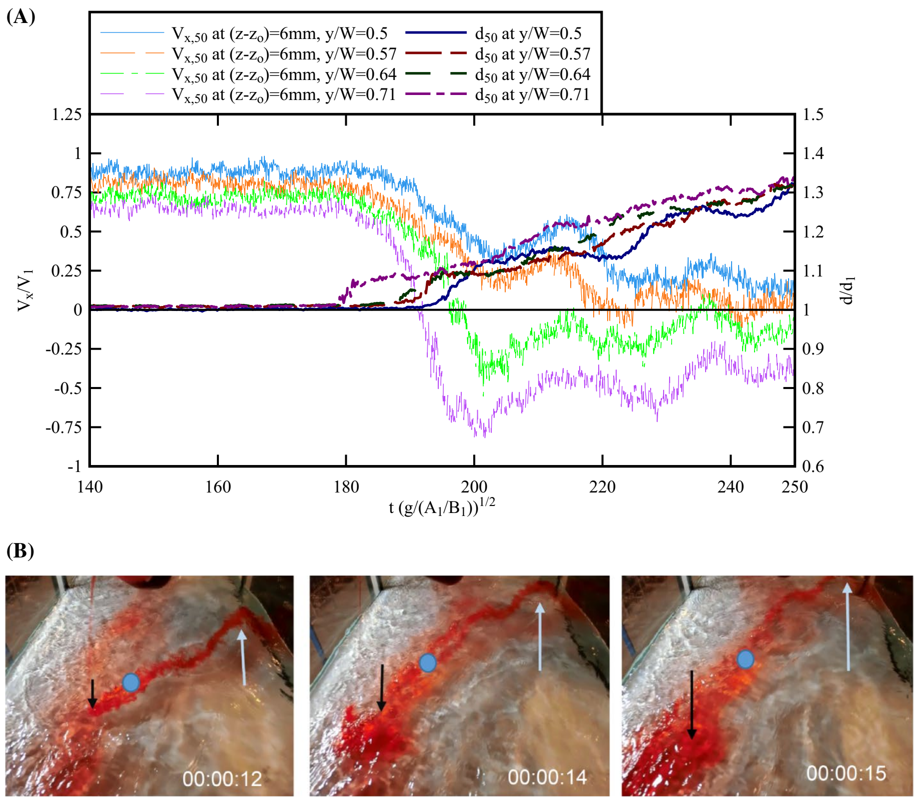

Fig. 8 Longitudinal velocity patterns at multiple transverse locations during positive surge passage for an initially triangular cross-section ($d_1/D<1$)—Flow conditions: $Fr_1=1.64$, $Q=0.030$ m^3/s and $h=0$ m. **a** Time variation of ensemble-median longitudinal velocity and water elevation at multiple transverse locations and $x=8.6$ m during positive surge passage. **b** Longitudinal flow motion during the propagation of the positive surge for $d_1/D<1$ highlighted using red dye injection—Looking downstream at about and $x=8.6$ m, with surge propagation from background to foreground and shallow-water section on the left—Blue dot marks location of transient shear zone

passage of the bore but with a less clearly observable peak. A similar trend was observed for the vertical and transverse velocity fluctuations, but with lower magnitude [21].

Across the channel width, the fluctuation in velocity components increased in magnitude towards the shallow-water section. For all results, the peak in velocity fluctuations occurred next the bed shortly after the passage of the bore front, rather than at the greatest rate of change in the free-surface elevation.

6 Unsteady flow properties. (2) turbulent Reynolds stresses

6.1 Presentation

The normal Reynolds stress components, $\rho v_x v_x$, $\rho v_y v_y$, $\rho v_z v_z$, and tangential Reynold stress components, $\rho v_x v_y$, $\rho v_z v_y$, $\rho v_x v_z$, were calculated from the ensemble-average data [10].

Herein, the median $(\rho v_i v_j)_{50}$ and fluctuation in the stress components $(\rho v_i v_j)_{75-25}$ were analysed for each experimental flow condition.

The passage of the positive surge had a marked effect on the turbulent Reynolds stresses. Figures 9 and 10 present typical time-variations of median and fluctuation of tangential $v_x v_x$ and normal $v_x v_y$ Reynolds stress components for two different flow conditions. In Figs. 9 and 10, $(v_i v_j)_{50}/V_1$ is the dimensionless ensemble-median Reynolds stress component, $(v_i v_j)_{75-25}/V_1$ is the Reynolds stress component fluctuation defined in terms of the inter-quartile range, d_{50}/d_1 is the dimensionless ensemble-median water elevation. The arrival of the compression wave front was followed by a sharp increase in all Reynolds

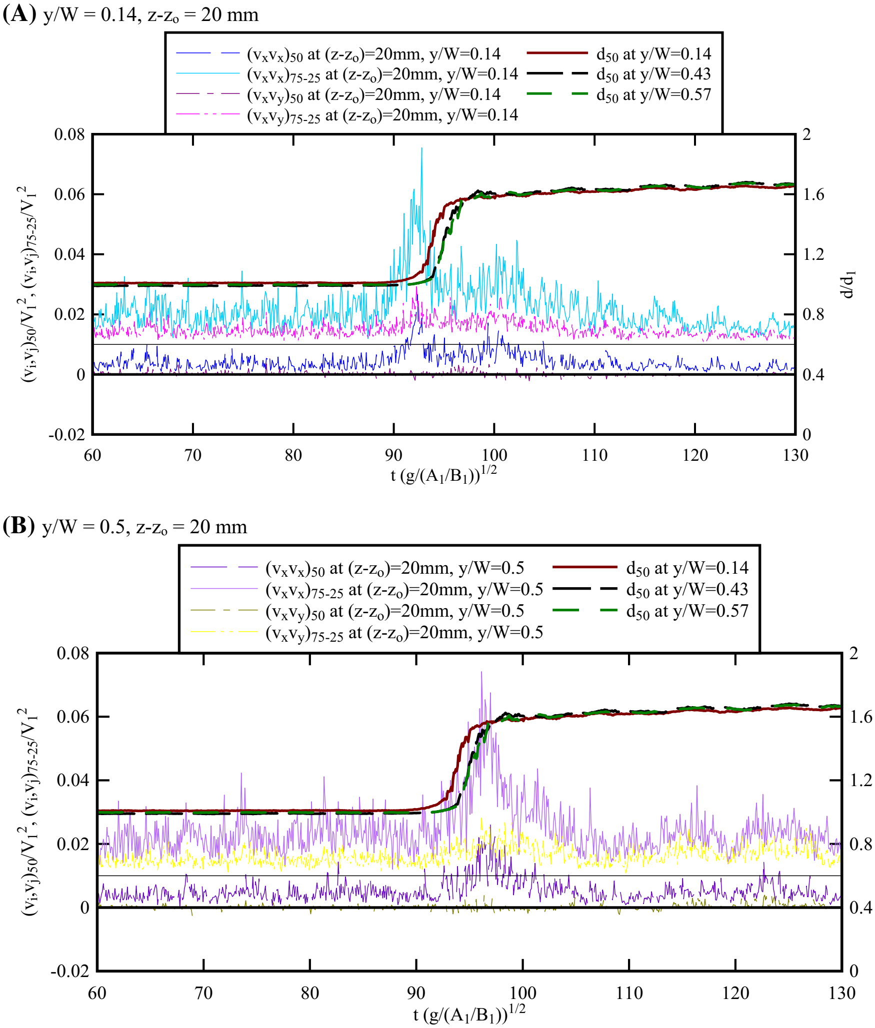

Fig. 9 Dimensionless time variations of Reynolds stress components $v_x v_x/V_1^2$ and $v_x v_y/V_1^2$, ensemble-median and fluctuations, at several transverse locations (fluctuation data offset by + 0.01) and x = 8.6 m—Flow conditions: Q = 0.1017 m^3/s, h = 0 m, Fr_1 = 1.60–1.80. **a** y/W = 0.14, z-z_o = 20 mm. b y/W = 0.5, z-z_o = 20 mm

(A)

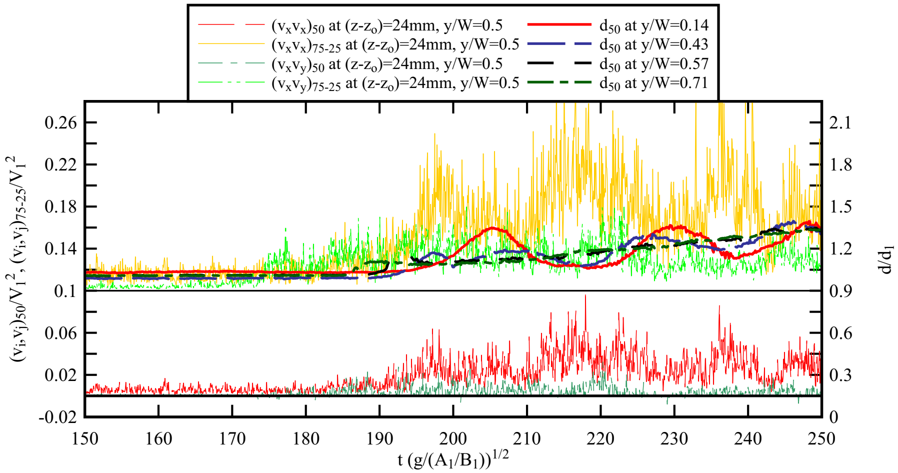

(B)

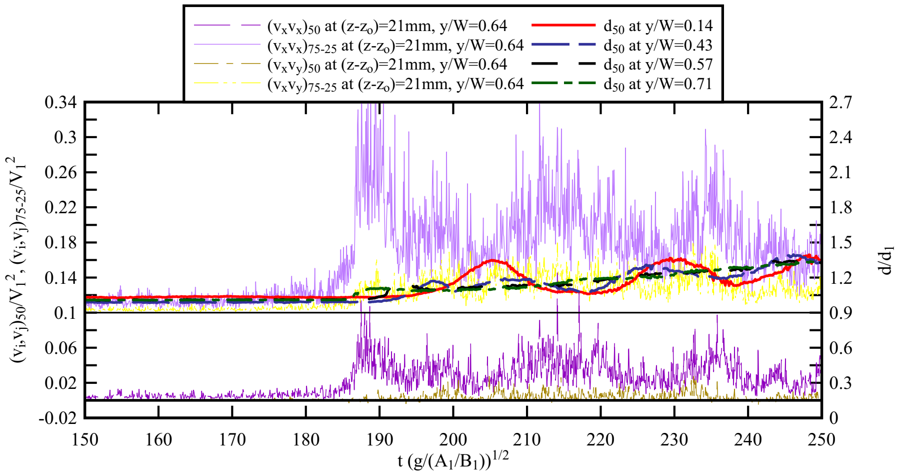

Fig. 10 Dimensionless time variations of Reynolds stress components v_xv_x/V_1^2 and v_xv_y/V_1^2, ensemble-median and fluctuations, at several transverse locations (fluctuation data offset by +0.1) and x = 8.6 m—Flow conditions: Q = 0.030 m^3/s, h = 0 m, Fr_1 = 1.61–1.65—Note different vertical axis scales between Fig. 8a and b. **a** y/W = 0.5, z-z_o = 24 mm. **b** y/W = 0.64, z−z_o = 21 mm

stress components, for all flow conditions. The Reynolds stress magnitudes were larger close to the bed than next the free-surface. That is, there was a well-defined peak in the shear stress amplitude next to the bed, whereas closer to the surface, the stress components showed a more gradual increase. The shear stress fluctuations showed also large values next the bed, roughly corresponding to the median shear stress maxima. Close to the water surface, the fluctuations in shear stress also showed a more gradual increase, with a pattern similar to that observed for the median shear stress. Generally the trend was consistent with previous observations in positive surges propagating in rectangular channels [5, 24, 25].

Within the experimental flow conditions (Table 1), the measured median stresses and shear stress fluctuations tended to increase with decreasing initial depth d_1/D. This is illustrated by comparing Figs. 9 and 10, corresponding respectively to $Q=0.10$ m^3/s and 0.030 m^3/s respectively. In comparing results for $Q=0.1017$ m^3/s ($d_1/D>1$) and $Q=0.030$ m^3/s ($d_1/D<1$), the median Reynolds shear stress amplitude was nearly an order of magnitude larger for $Q=0.030$ m^3/s and $d_1/D<1$, after the bore passage. This derived from an increasing effect of the transverse slope in the shallower cross-section, inducing complex secondary currents and flow patterns. Further, the magnitude of the Reynolds stresses and Reynolds stress fluctuations tended to be the largest about the channel centreline ($y/W \sim 0.5$), likely caused by the complex redistribution in velocity across the channel, This was particularly evidenced for $Q=0.030$ m^3/s and $d_1/D<1$, for which the maximum median shear stresses and shear stress fluctuations about the channel centreline were nearly an order of magnitude larger than in the deep-water section (Fig. 10).

6.2 Transient secondary motion and shear plane

The present results in the asymmetrical channel showed significantly higher Reynolds stress levels, in comparison to previous studies in a rectangular channel (e.g. [24, 25]. This was an indication of higher turbulent shearing and mixing induced by the passage of the surge as a result of the asymmetrical bed topography.

For $d_1/D<1$ and $Q=0.030$ m^3/s, both velocity and shear stress data showed the existence of a marked transient longitudinal x–z shear surface, about y/W 0.5–0.6, along which strong secondary motion and shear stress occurred behind the surge. This shear plane is illustrated in Fig. 3b and c in red. The secondary motion was not unlike secondary motion in steady flows in compound channels [23, 31, 39], albeit the present data showed that the secondary motion was transient and very intense. Large transverse velocity and velocity fluctuations were observed during and shortly after the compression wave passage. In the shear plane y/W 0.5–0.6, high Reynolds stress magnitudes and shear stress fluctuations were observed behind the surge. Quantitatively, shear stress amplitude $|(\rho v_i v_j)_{50}|$ in excess of 40 Pa and shear stress fluctuations $(\rho v_i v_j)_{75-25}$ larger than 150 Pa were recorded in the present study. Such values of median shear stress magnitudes were one to two orders of magnitude larger than boundary shear stress levels in steady flow conditions [21] and steady flow measurements in compound channels (e.g. [31]).

The present findings were obtained in a prismatic non-rectangular asymmetrical channel. They may further apply to positive surge propagation in prismatic symmetrical trapezoidal and triangular channels. Secondary motion down the side slope is likely to be observed behind compression waves, with intense shear stresses about mid-slope.

7 Conclusion

An investigation of compression waves was conducted in a prismatic asymmetrical channel, to better understand the physical processes observed in tidal/tsunami-bore affected estuaries with irregular topography. The physical modelling was based upon geometric, Froude and Morton similitudes of a prismatic channel equipped with a 1 V:5H transverse slope across the whole channel width. The physical observations behave much as theoretically derived forced flow patterns.

The unsteady surge flow pattern was a function of both Froude number Fr_1 and relative initial flow depth d_1/D. The free-surface data presented three-dimensional unsteady flow features. The velocity measurements showed a drastic impact of the surge on the flow field, with strong three-dimensional features in the asymmetrical channel. The compression wave passage induced a rapid flow deceleration, and large and rapid fluctuations of all velocity components behind the compression wave. A key feature was the three-dimensional nature of the surge front in the asymmetrical non-rectangular flume. The experimental results showed a transient three-dimensional flow associated with some transverse mixing induced by unsteady secondary motion. With the arrival of the surge front and for all flow conditions, the transverse velocity component became large in the shallow-water section, indicating some unsteady secondary motion and recirculation during and shortly after the passage of the surge. Fluctuations in all velocity components increased markedly following the arrival of the bore surge. A sizeable peak in velocity fluctuations was consistently observed in the lower water column. The Reynolds shear stress data showed that the arrival of the bore was associated with large turbulent stresses and shear stress fluctuations. For all flow conditions investigated, the measured median Reynolds stresses increased with decreasing initial depth. For experiments conducted with $d_1/D < 1$, both velocity and shear stress data showed a transient longitudinal x–z shear plane was observed about y/W 0.5–0.6, with conjugate transverse flow reversal observed for $0.5–0.6 < y/W < 1$ (Fig. 3B). In the transient shear plane, high Reynolds stress magnitudes and shear stress fluctuations were observed behind the surge front, up to one to two orders of magnitude larger than boundary shear stress levels observed in steady flows in compound channels.

Overall the unsteady turbulent field presented marked differences in comparison to observations in rectangular channels. The findings may be directly relevant to surge propagation in natural irregular-shaped channels and man-made trapezoidal waterways in terms of numerical modelling. Classical depth-averaged numerical models, e.g. based upon St Venant equations and Boussinesq equations, are inadequate to model the complicated three-dimensional turbulent motion beneath surges in irregular channels. A full three-dimensional computational fluid dynamics (3D CFD) model based upon the Navier–stokes equations is required, albeit a proper validation is critical and necessitates suitable, high-quality physical modelling data [27, 30].

8 Appendix I: Digital appendix

Visual observations of the experiments were carried out using a digital camera Casio™ Exilim EX10. The movie (file CIMGP3470.mov, duration: 113 s) was recorded at 120 fps (resolution: 640px × 480px) and it is replayed at 30 fps. The movie shows the three-dimensional propagation of the compression wave for the following flow conditions: $Q = 0.03$ m^3/s, $S_o = 0.002216$, $Fr_1 = 1.6–1.7$, $d_1/D = 0.93$. Dye injection starting at 15 s emphasises the complicated three-dimensional conjugate flow motion, with the conjugate flow direction positive (i.e. downstream) in the deep-water section and negative (i.e. upstream) in the shallow-water section of the channel.

Acknowledgements The authors thank Professor Rollin HOTCHKISS (Brigham Young University, USA) and Dr Oscar CASTRO-ORGAZ (University of Cordoba, Spain) for their valuable comments. X.L. and H.C. acknowledge the helpful inputs of Professor Pierre LUBIN (University of Bordeaux, France). The authors are grateful for the constructive comments of the associate editor and two reviewers. The technical assistance of Jason VAN DER GEVEL and Stewart MATTHEWS (The University of Queensland, Australia) is greatly appreciated. The financial support of the Australian Research Council (ARC DP120100481) and of the School of Civil Engineering, the University of Queensland is acknowledged.

References

1. Barré de Saint-Venant AJC (1871) Théorie du Mouvement Non Permanent des Eaux, avec Application aux Crues des Rivières et à l'Introduction des Marées dans leur Lit. Comptes Rendus des séances de l'Académie des Sciences 73(4):147–154 **(in French)**
2. Barré de Saint-Venant AJC (1871) Théorie et Equations Générales du Mouvement Non Permanent des Eaux, avec Application aux Crues des Rivières et à l'Introduction des Marées dans leur Lit (2ème Note). Comptes Rendus des séances de l'Académie des Sciences, Paris, France, Séance 17 73:237–240 **(in French)**
3. Bazin H (1865) Recherches Expérimentales sur la Propagation des Ondes." ('Experimental Research on Wave Propagation'.). Mémoires présentés par divers savants à l'Académie des Sciences 19:495–644 **(in French)**
4. Benet F, Cunge JA (1971) Analysis of experiments on secondary undulations caused by surge waves in Trapezoidal channels. J Hydraul Res IAHR 9(1):11–33
5. Chanson H (2010) Unsteady turbulence in tidal bores: effects of bed roughness. J Waterway Port Coast Ocean Eng ASCE 136(5):247–256. https://doi.org/10.1061/(ASCE)WW.1943-5460.0000048
6. Chanson H (2011) Tidal Bores, Aegir, Eagre, Mascaret, Pororoca: theory and observations. World Scientific, Singapore, 220. ISBN: 9789814335416
7. Chanson H (2012) Momentum considerations in hydraulic jumps and bores. J Irrig Drain Eng ASCE 138(4):382–385. https://doi.org/10.1061/(ASCE)IR.1943-4774.0000409
8. Chanson H (2014) Applied hydrodynamics: an introduction. CRC Press, Taylor & Francis Group, Leiden, The Netherlands, 448 pages & 21 video movies
9. Chanson H (2020) Statistical analysis method for transient flows: the Dam-Break Case. discussion. Journal of Hydraulic Research, IAHR. https://doi.org/10.1080/0221686.2020.1729266. (In Print)
10. Chanson H, Docherty NJ (2012) Turbulent velocity measurements in open channel bores. Eur J Mech B/Fluids 32:52–58. https://doi.org/10.1016/j.euromechflu.2011.10.001
11. Chanson H, Reungoat D, Simon B, Lubin P (2011) High-frequency turbulence and suspended sediment concentration measurements in the Garonne River Tidal Bore. Estuar Coast Shelf Sci 95(2–3):298–306. https://doi.org/10.1016/j.ecss.2011.09.012
12. Chow VT (1959) Open channel hydraulics. McGraw-Hill, New York
13. Csanady GT (1973) Wind-induced barotropic motions in long lakes. J Phys Oceanogr 3:429–438
14. Cunge JA, Holly FM Jr, Verwey A (1980) Practical aspects of computational river hydraulics. Pitman, Boston, p 420
15. Favre H (1935) Etude Théorique et Expérimentale des Ondes de Translation dans les Canaux Découverts. Theoretical and experimental study of travelling surges in open channels. Dunod, Paris, France (in French)
16. Furgerot L, Mouaze D, Tessier B, Perez L, Haquin S, Weill P, Crave A (2016) Sediment transport induced by tidal bores. An estimation from suspended matter measurements in the Sée River (Mont-Saint-Michel Bay, northwestern France). Comptes Rendus Géoscience, 10 p. doi:https://doi.org/10.1016/j.crte.2015.09.004. (In print)
17. Henderson FM (1966) Open channel flow. MacMillan Company, New York
18. Hornung HG, Willert C, Turner S (1995) The flow field downstream of a hydraulic jump. J Fluid Mech 287:299–316
19. Jaeger C (1956) Engineering fluid mechanics. Blackie & Son, Glasgow, UK, p 529
20. Keevil CE, Chanson H, Reungoat D (2015) Fluid flow and sediment entrainment in the Garonne River Bore and Tidal Bore Collision. Earth Surf Proc Land 40(12):1574–1586. https://doi.org/10.1002/esp.3735
21. Kiri U, Leng X, Chanson H (2018) Positive surge propagation in a non-rectangular asymmetrical channel. Hydraulic Model Report No. CH110/18, School of Civil Engineering, The University of Queensland, Brisbane, Australia, 159 pages and 2 digital appendices incl. 5 movies
22. Kjerfve B, Ferreira HO (1993) Tidal bores: first ever measurements. Ciência e Cultura (Jl of the Brazilian Assoc for the Advancement of Science) 45(2):135–138

23. Knight DW (2013) River hydraulics: a view from midstream. J Hydraul Res IAHR 51(1):2–18. https://doi.org/10.1080/00221686.2012.749431
24. Koch C, Chanson H (2009) Turbulence measurements in positive surges and bores. J Hydraul Res IAHR 47(1):29–40. https://doi.org/10.3826/jhr.2009.2954
25. Leng X, Chanson H (2016) Coupling between Free-surface Fluctuations, Velocity Fluctuations and Turbulent Reynolds Stresses during the Upstream Propagation of Positive Surges, Bores and Compression Waves. Environ Fluid Mech 16(4):695–719. https://doi.org/10.1007/s10652-015-9438-8
26. Leng X, Chanson H (2017) Integral turbulent scales in unsteady rapidly varied open channel flows. Exp Thermal Fluid Sci 81:382–395. https://doi.org/10.1016/j.expthermflusci.2016.09.017
27. Leng X, Simon B, Khezri N, Lubin P, Chanson H (2018) CFD modelling of tidal bores: development and validation challenges. Coast Eng J 60(4):423–436. https://doi.org/10.1080/21664250.2018.1498211
28. Liggett JA (1994) Fluid mechanics. McGraw-Hill, New York
29. Lighthill J (1978) Waves in fluids. Cambridge University Press, Cambridge, p 504
30. Lubin P, Chanson H (2017) Are breaking waves, bores, surges and jumps the same flow? Environ Fluid Mech 17(1):47–77. https://doi.org/10.1007/s10652-016-9475-y
31. Macintosh JC (1990) Hydraulic characteristics in channels of complex cross-section. Ph.D. thesis, University of Queensland, Department of Civil Engineering, Australia, November, 487 p. doi:https://doi.org/10.14264/uql.2015.218
32. Montes JS (1998) Hydraulics of open channel flow. ASCE Press, New-York, p 697
33. Montes JS, Chanson H (1998) Characteristics of undular hydraulic jumps. results and calculations. J Hydraul Eng ASCE 124(2):192–205. https://doi.org/10.1061/(ASCE)0733-9429(1998)124:2(192)
34. Nezu I, Rodi W (1985) Experimental study on secondary currents in open channel flow. In: Proceedings 21st IAHR Biennial Congress, Melbourne, Australia, pp 114–119
35. Reungoat D, Leng X, Chanson H (2016) Hydrodynamic and sedimentary processes of tidal bores: Arcins Channel, Garonne River in August-September-October 2015. Hydraulic Model Report No. CH102/16, School of Civil Engineering, The University of Queensland, Brisbane, Australia, 270 pages. ISBN 978–1–74272–155–2
36. Rouse H (1938) Fluid mechanics for hydraulic engineers. McGraw-Hill Publ., New York (also Dover Publ., New York, USA, 1961, 422 p)
37. Sandover JA, Taylor C (1962) Cnoidal waves and bores. J La Houille Blanche, No. 3, Sept., pp 443–445
38. Schlichting H (1979) Boundary Layer Theory, 7th edn. McGraw-Hill, New York
39. Shiono K, Knight DW (1991) Turbulent open channel flows with variable depth across the channel. J Fluid Mech 222: 617–646 (& Vol. 231, p. 693)
40. Spiegel MR (1972) Theory and problems of statistics. McGraw-Hill Inc., New York
41. Stoker JJ (1957) Water waves: the mathematical theory with applications. Interscience Publishers, New York, p 567
42. Tamburrino A, Gulliver JS (2007) Free-surface visualization of streamwise vortices in a channel flow. Water Resour Res 43, Paper W11410, p 12. Doi: https://doi.org/10.1029/2007WR005988
43. Tanaka H, Tinh NX, Dao NX (2011) Field measurement and numerical studies on the Tsunami propagation into upstream rivers. In: Proceedings of 34th IAHR World Congress, Brisbane, Australia, 26 June-1 July, Engineers Australia Publication, Eric VALENTINE, Colin APELT, James BALL, Hubert CHANSON, Ron COX, Rob ETTEMA, George KUCZERA, Martin LAMBERT, Bruce MELVILLE and Jane SARGISON Editors, pp 1317–1324
44. Trevethan M, Chanson H, Brown R (2008) Turbulence characteristics of a small subtropical estuary during and after some moderate rainfall. Estuar Coast Shelf Sci 79(4):661–670. https://doi.org/10.1016/j.ecss.2008.06.006
45. Yasuda H (2010) One-dimensional study on propagation of tsunami wave in river channels. J Hydraul Eng ASCE 136(2):93–105

Publisher's Note Springer Nature remains neutral with regard to jurisdictional claims in published maps and institutional affiliations.